Reaction Chemistry & Engineering

PAPER

Check for updates

LearnCK: mass conserving neural network reduction of chemistry and species of microkinetic models†

Sashank Kasiraju [iD][a] and Dionisios G. Vlachos [iD] *[ab]

Reduction of chemical reaction mechanisms has been long studied to minimize the computational cost of reacting flows or the number of parameters of catalytic reaction models for estimation from experimental data. Conventional reduction techniques encompass either a tabulation of the reaction rates of elementary reactions or a reduction of elementary reactions. We introduce a Python-TensorFlow tool to learn chemical kinetics (LearnCK) systematically and automatically from microkinetic models using artificial neural networks (NNs). The approach constructs overall reactions among stable species only and interconversion rates and dramatically reduces the number of species and, thus, of the differential equations (the most expensive aspect in reacting flows). Doing this also removes the stiffness and nearly eliminates the complexity and cost of estimating the entire thermochemistry and kinetic rate expressions for computing reaction rates. Python programming automates training data generation, extracts metadata for fitting the NNs, and deploys the NN model. Since NNs are black boxes, we propose an approach to conserve mass. We demonstrate the method for the ammonia synthesis on Ru and the methane non-oxidative coupling over a single-atom Fe/SiO$_2$ catalyst. The latter model includes over 500 gas and surface species and a combined 9300 gas and surface reactions. We demonstrate a nearly 1000-fold computational speedup and exceptional predictive accuracy using up to 8 overall reactions. The NN model is embedded in macroscopic reactor flow models to estimate uncertainty.

1. Introduction

Microkinetic models (MKMs) of complex homogeneous and heterogeneous reaction mechanisms have become commonplace.[1–8] The conservation species equations of chemical kinetics are highly nonlinear and stiff, require specialized solvers and expertise, and are costly for large reaction mechanisms. As a result, their penetration to reacting flow simulators, such as computational fluid dynamics (CFD), and systems tasks, such as optimization and control, has been slow.[9–13] An overview of the current strategies and challenges in the application of CFD to reactive flows has been discussed.[14,15]

The computational singular perturbation method was introduced thirty years ago to remove stiffness of chemical kinetics and potentially reduce the network.[16] Optimization

has also been employed as a mathematical programming-based rigorous approach to eliminate inconsequential reactions based on preset performance metrics.[17–19]

In chemical reaction engineering, mechanism reduction has often been employed to mitigate numerical complexity, improve computational tractability, and better understand the overall reaction. A key approach has employed the separation of time scales by identifying key species and rate-limiting step(s). Common approaches involve local sensitivity analysis (LSA), principal component analysis (PCA), reaction path analysis (RPA), quasi-steady-state (QSS), partial equilibrium (PE) analysis, and most abundant surface intermediates (MASI).[20,21] For catalytic MKMs, our group has applied *a posteriori* mechanism reduction where MASIs, RDS, *etc.* are determined after the solution has been obtained. Simple order 1 asymptotics have then been used to derive closed-form rate expressions that are consistent with the MKM physics. These expressions expose all the fundamental reaction rate and equilibrium constants and are interpretable (in the AI nomenclature). These often entail pencil and paper calculations.[22–25] Aside from reducing detailed mechanisms, *a priori* assumptions, such as the RDS, PE, QSS, and MASI, have been commonplace in catalysis to create overall rate expressions for comparison to experiments, mechanism

*[a] RAPID Manufacturing Institute and Delaware Energy Institute, University of Delaware, 221 Academy St., Newark, Delaware 19716, USA.
E-mail: vlachos@udel.edu*
[b] Department of Chemical and Biomolecular Engineering, University of Delaware, 150 Academy St., Newark, Delaware 19716, USA

† Electronic supplementary information (ESI) available: This document lists several figures and tables with data mentioned in this paper. See DOI: https://doi.org/10.1039/d3re00279a

discrimination, and parameter estimation. The famous Langmuir–Hinshelwood–Hougen–Watson (LHHW) models are a manifestation of this approach.

In a complementary pioneering approach of Pope, the *in situ* adaptive tabulation (ISAT)[26,27] method that tabulates the rates of elementary reactions on the fly of a simulation has generated intensive research. The combustion community has extensively used it to accelerate CFD simulations of chemically reacting flows.[27–29] For every simulation at runtime, the reaction rate table is built by running the full MKM. The table can become large and inefficient; for unseen conditions, the MKM must be used to update the table.[30] ISAT does not reduce the size and stiffness of the system. It eliminates the computation of reaction rates by interpolating within the reaction rates table and, by doing this, it saves considerable computational time. The technique has been applied to other problems, *e.g.*, kinetic Monte Carlo simulations[31,32] and real-time control.[33]

Neural networks (NNs) are universal function approximators[34,35] of high-dimensional nonlinear functions that can be ideal surrogates of chemical kinetics. The combustion research community has embraced NNs to tackle several challenges in the temporal evolution of standalone complex kinetic models or in conjunction with CFD simulations. Some examples include modeling the temporal evolution of a reduced combustion chemical system,[36] large-scale eddy simulations of turbulent flames,[37–39] machine learning in reaction flow CFD,[40] and on-the-fly NN-based numerical integration for combustion.[41] Recently several articles described specialized applications embedding NNs inside numerical integrators to describe the time evolution of ordinary differential equations (ODEs) describing the chemical kinetics of reacting species. Firstly, kinetics-informed NN[42] and chemical reaction NN (CRNN)[43] describe NN frameworks that satisfy physical constraints and design equations set by the ODEs describing chemical reaction systems and can be used to elucidate reaction mechanisms and pathways from experimental data. ChemNODE,[44] a new type of NN named neural ordinary differential equations (NODEs),[45] is computationally efficient but has not been demonstrated for stiff systems. Physics-informed NN-based models (PINN) do not perform well for stiff ODEs;[46,47] alternatives such as stiff-PINN[48] and MPINN[46] were developed to alleviate stiffness. Stiff-PINN[48] reduces the system complexity by ignoring short-lived species with the quasi-steady-state approximation. The resulting DAEs must be hand-calculated on a case-by-case basis; MPINN[46] employs multiple PINNs to handle species with different time scales, but it is not clear how the method handles very large systems. A residual NN (ResNet)-based deep NN model called KiNet[49] employs several deeply stacked ResNets (in the stack each time step requires an independent ResNet) for efficient backward propagation through time networks. However, due to the very deep stacking of multiple ResNets, the computational complexity and memory required depend on the number of time steps, and it is unclear how the method

scales with system size (number of individual species tracked). More recently, NNs and multivariate spline interpolation were used to approximate reduced-order MKMs constructed using traditional methods such as the partial equilibrium index and the degree of rate control.[50] In this approach forward, backward, and net rates of elementary reactions (of the reduced model) were captured using a latent asinh[51] and logarithmic[50] transformation. Finally, a method augmenting a modification of CRNNs with an Euler integrator to model stiff atmospheric chemistry[52] was developed, where the adaptive time step of integration is estimated from the NNs eliminating the need to calculate computationally expensive Jacobians. All these methods solve the complete high-dimensional problem or the reduction of the problem to a lower dimensional manifold (Stiff-PINN) requires hand-calculations and is not scalable to very large reaction networks.

Here, we propose a new detailed kinetic model reduction using deep NNs (DNNs) without analysis, tabulation, or human intervention. We only consider key reactants and products seen in experiments, and track 'user-defined' rates of a handful of overall reactions connecting these species. The approach is both computationally efficient, as it reduces both reactions and species and removes stiffness, and is also a tabulator, as it parametrizes rates *vs.* the local reactor conditions. We first describe the procedure used to generate training data, fit the NNs, and then deploy them within numerical integrators as surrogates in reactor models. We discuss the implications of mass conservation as NNs do not follow physical laws *a priori* and quantify the uncertainty resulting due to the errors. The entire methodology is tested on a proof-of-concept MKM system (NH_3 decomposition to N_2 and H_2, with a total of 18 gas and surface species and 14 surface reactions) and a very complex MKM model (methane coupling to C2–C10 products, with over 500 species and *ca.* 9300 gas- and surface-phase reactions).

2. Methods

2.1 The model reduction workflow

The algorithm entails the following steps: a) identification of the phase space and quantities of interest (QoIs), b) generation of training data (within the operating window) using Latin hypercube sampling (LHS)-based full-order MKM simulations, c) processing and transformation of the training dataset, d) construction and training of the DNNs, e) construction of an NN surrogate-based numerical integrator (reduced model), and f) evaluation, validation and uncertainty quantification (UQ) of the reduced model and the underlying NN. The outline of the workflow is shown in Fig. 1. We describe each of the steps and the overall algorithm next.

2.2 Phase-space and QoI identification

First the phase-space of operating conditions, such as temperature, pressure, feed flowrate, feed composition,
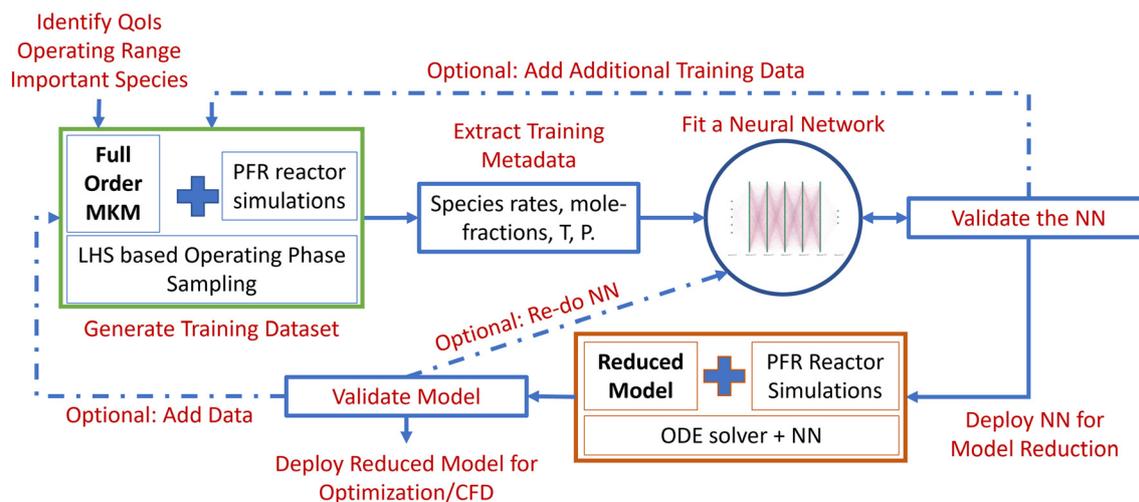
Fig. 1 LearnCK model reduction workflow.

residence time, *etc.*, is defined, so that the NN can reliably predict within it. For a large full-order MKM system with hundreds of species (short-lived intermediates and long-lived reactants and products), we need to identify long-lived species which contribute the most to the reactor concentration (see the example of methane chemistry). The key QoIs which need to be predicted by the NN-integrated reduced model are defined (*e.g.*, species concentrations or conversion or selectivity).

2.3 Creating the dataset

We perform plug flow reactor (PFR) simulations by approximating a PFR as a series of 100 CSTRs; each CSTR in a single simulation serves as an independent datapoint of a different local composition (and potentially a different temperature and pressure) within this phase-space using sampling methods, such as LHS. Each PFR simulation provides the low-dimensional manifold of chemical kinetics staring from the initial conditions and moving toward equilibrium downstream. The dataset comprises data from several hundred PFR simulations, each providing 100 datapoints. PFR simulations of large reaction networks are feasible, not as time consuming, and robust.

2.4 Data transformation

The input features required by the NNs in this work are local concentration of (selected) species, temperature, and pressure; the output responses are turnover frequencies (sometimes normalized using the log 10 scale). These input features are scaled using a MinMaxScaler,[53] such that each feature has a maximum value of 1.0 and a minimum value of 0.0:

$$X_{\text{new}} = \frac{X - \min(X)}{\max(X) - \min(X)} \times (1.0 - 0.0) + 0.0, \tag{1}$$

where X_{new} is the scaled dataset, X is the original dataset, $\min(X)$ is the dataset minimum, and $\max(X)$ is the dataset

maximum. Alternatively, the dataset is normalized using the TensorFlow's preprocessing normalization layer,[54] which centers each feature around a mean of 0 and a standard deviation of 1:

$$X_{\text{new}} = \frac{X - \overline{X}}{\sqrt{\text{Var}(X)}} \tag{2}$$

where X is the set of data for a given feature, $\overline{X}$ is the mean, $\text{Var}(X)$ is the variance, and X_{new} is the normalized dataset.

The predicted targets using a NN could include turnover frequencies (TOFs), steady-state rates, conversion, selectivity, *etc.* In this work on heterogeneous catalytic models, TOFs are chosen which only depend on the temperature, pressure, and local composition of reactants and products for a given catalyst and are agnostic to feed flowrate and residence time. Depending on the order of magnitude of TOFs in the training dataset, they are sometimes represented in the log 10 scale to ensure very low rates are accounted for accurately. The dataset is split randomly 70 : 30 into training and testing sets, respectively.

2.5 Construction and training of the NN

The input features required by the NNs in this work are local concentration of (selected) species, temperature and pressure and the output responses are TOFs (sometimes normalized using the log 10 scale). TensorFlow[55] was used to construct a simple feed-forward DNN. Overfitting is suppressed with early stopping, which stops network training when the loss-function does not improve, after a pre-defined number of epochs. While the entire architecture of the DNN, *i.e.*, layer depth, number of neurons in each layer, combinations of activation functions, regularization, and dropout penalty, can be custom designed and improved using hyper-parameter optimization, the networks described here are simple and homogeneous (only one type of activation function and the same number of neurons in each layer) to demonstrate

This journal is © The Royal Society of Chemistry 2024

React. Chem. Eng., 2024, **9**, 119–131 | **121**

feasibility of the concept. DNNs in this work are typically 5 layers deep, with 50 neurons in each layer, and use an identical activation function, either rectified linear units (ReLU)[55,56] or Gaussian error linear unit (GELU).[55,57]

The choice of hyper-parameters could have an effect on the NN performance as shown for a couple of parameters in Fig. S3† (activation function) and Fig. S4† (hidden layer depth), but the difference is negligible. However, we note that the NN architecture considered in this work might not be ideal for all chemically reacting systems and therefore appropriate hyper-parameter optimization must be carefully performed for optimal results. The tunable parameters within the DNN are fitted *via* the well-regarded stochastic gradient descent method, Adam optimizer offered by the TensorFlow library, with a learning rate of 0.001, using the mean absolute error (MAE) loss metric for the objective function evaluated for the entire training dataset (between the TOFs predicted by the DNNs and MKM simulations).

2.6 DNN-surrogate-based PFR numerical simulations

The Python-SciPy stiff ODE solver *solve_ivp*,[58] specifically the *LSODA*[59,60] algorithms, is employed to numerically solve the steady-state PFR simulation using the DNN reaction rates. The Jacobian matrix is approximated with finite differences using the default implementation within the SciPy *solve_ivp*[58] solver. The governing equations for a detailed or a coarse-grained kinetic model are

$$\frac{\mathrm{d}C_j}{\mathrm{d}x} = \sum_{i=1}^{n} S_{j,i} \times r_i(T, P, X) \qquad (3)$$

$$\frac{\mathrm{d}C_j}{\mathrm{d}x} = \sum_{j=1}^{m} \sigma_j(T, P, X) \qquad (4)$$

where $\frac{\mathrm{d}C_j}{\mathrm{d}x}$ is the rate of change of concentration of species j along a differential length ($\mathrm{d}x$), $S_{j,i}$ is the stoichiometric coefficient of species j in elementary reaction i, and $r_i(T, P, C)$ is the rate of elementary reaction i at the current pressure (P), temperature (T), and composition (X). The summation extends over the entire networks of n elementary reactions. Similarly, $\sigma_j(T, P, X)$ is the rate of species j from all overall reactions j and the summation extends over all overall reactions m. In a MKM simulator, the elementary rate is expressed by the modified Arrhenius rate expression, and the species rate is calculated using the elementary rates and the stoichiometry matrix. The DNNs can approximate the species production rate, *i.e.*, the entire rhs (see ammonia case-study) or the overall reaction rates (see methane case-study), by accepting identical inputs (T, P, X). Note that DNNs are black boxes which could predict species consumption even when the species concentration is zero, resulting in negative concentrations. Therefore, in the coarse-grained kinetic model we ensure that the species mass and mole balances are always positive by constraining the species conservation equations and clipping rates which result in negative concentrations.

The DNN-surrogate-based PFR model does not involve surface species and their coverages, and, therefore, one does not need initial conditions for surfaces. One only needs inlet concentrations of gas reactants.

2.7 Validation and UQ for the NN-surrogate and the reduced model

The difference between the output responses, *i.e.*, the point predictions of TOFs by the NN-based model and the full-order MKM (training dataset), gives the necessary validation and UQ for the NN. This can be used to improve the NN architecture by performing hyper-parameter optimization or updating the training dataset. Similarly, the difference between the MKM and NN-based solutions (QoI) along a PFR provides the actual error of the reduced model *vs.* the full-order model.

To summarize, we generate a training dataset within the operating conditions window by running multiple PFR simulations with the full MKM. The training dataset consists of local operating conditions, species concentrations, and either species rates or rates of overall reactions. The training dataset is fitted with a DNN which accepts local operating conditions and species concentrations to predict overall reaction on species rates. PFR simulations accept the trained DNN as a surrogate model for the full MKM. Since the DNN-based PFR model only tracks the long-lived gas-phase species *via* overall reactions connecting them, neither surface coverages nor elementary reactions are invoked, an important difference from previously published work.[50] This approach results in significant calculation speedup while eliminating stiffness. This workflow is demonstrated using two examples: a) a simple ammonia chemistry model where rates of production/consumption of each of the species are related *via* stoichiometry and b) the complex methane coupling chemistry with 9000+ elementary reactions.

2.8 Ammonia (NH₃) chemistry

The MKM for NH_3 decomposition on Ru has a total of 18 gas and surface species and 14 surface reactions (it entails step and terrace sites) and is taken from our previous work.[1,61,62] The species and reactions are given in Section ESI-1.† The training data were generated using OpenMKM[63] for a PFR (length of 1 cm, volume of 1 cm³) using LHC sampling for pressures from 1 to 10 atm, temperatures between 600 and 1000 K, and volumetric flow rates between 0.01 and 0.20 cm³ s⁻¹. The predicted output metrics are the TOFs of NH_3, N_2 and H_2. In the training dataset, the TOFs spanned several orders of magnitude: $\sim 10^{-10}$–10^2 (1 s⁻¹). Since there is only one overall reaction, the TOFs of the stable species are related by stoichiometry. However, TOFs of all three species were trained to assess how well mass-conservation is obeyed without imposing it. A total of 1200 conditions were simulated, and 100 training points were extracted from each reactor. DNN used 5 input parameters (T, P, X_{NH_3}, X_{N_2}, X_{H_2}), where X_i is the mole fraction of species i. Fig. S1 and S2a†

122 | *React. Chem. Eng.*, 2024, **9**, 119–131

This journal is © The Royal Society of Chemistry 2024

depict the nodes and connections in this NN. The training and validation error as a function of training epochs is plotted in Fig. S2b,† with training and validation errors decreasing steadily.

2.9 Methane (CH$_4$) coupling chemistry

Methane coupling to ethylene and other products is a complex network with 47 surface species, over 500 gas-phase species and a total of ~9300 gas- and surface-phase reactions.[64] The training data used 200 operating conditions picked *via* LHS, within the phase boundaries of (P = 1 atm, temperature 1250 to 1300 K, and volumetric flow rate of 0.025 to 1 cm^3 s^{-1}) using the CHEMKIN[65–67] chemical kinetics package. Mole fractions and TOFs of key species were obtained from these simulations. Only species which contributed cumulatively to 99.9% of the mole fraction (with decreasing contribution) are considered; these are CH$_4$, H$_2$, C$_2$H$_2$, C$_2$H$_4$, C$_2$H$_6$, C$_3$H$_4$, C$_3$H$_6$, C$_6$H$_6$, C$_7$H$_8$, and C$_{10}$H$_8$. To preserve mass and enforce stoichiometry on top of the black-box DNNs, overall reaction TOFs instead of species TOFs are fitted. These overall reactions are constructed to connect the species using expert knowledge as explained below in the section "overall reactions". While the DNN model predictions of overall reaction rates have errors, stemming from the reduction, mass is conserved as we parametrize reaction rates and use stoichiometry to compute all species rates. The NN architecture, sampling, and the PFR simulation numerics remain the same for both example cases. The simplicity and automation of various steps, *via* modular Python programming, enabled trivial scale-up of the methodology from the simple 14-reaction system to the ~9300 reactions.

3. Results and discussion

3.1 Assessing accuracy and training procedures using ammonia chemistry as a testbed

The training dataset was generated using OpenMKM[63] with the procedure and operating condition window described in the Methods section. DNNs were trained on the TOF of NH$_3$, and the TOFs of H$_2$ and N$_2$ were estimated from the stoichiometry of the overall reaction (2NH$_3$ ⇌ N$_2$ + 3H$_2$). Fig. 2a depicts the parity plot from the MKM and the DNN. DNNs display excellent performance with R^2 of 0.9997; the prediction error and mean were ~0.001 and ~0.002 in TOF units. This surrogate model performed well for reactor calculations. Fig. S5† depicts the parity in the exit mole fractions of 1200 independent PFR simulations (ground-truth) and the DNN surrogate, with a mean absolute error of ~0.0048 (dimensionless units).

3.1.1 Distance from equilibrium. Many reactions are equilibrium limited, and thus sampling at sufficiently long residence times leads to near equilibrium. Such conditions lead to performance deterioration because the net rates are very small, and effectively one adds noise to the dataset. For this reason, during the PFR integration, the distance from equilibrium was assessed (using an L2 norm) at each pressure and temperature. Below a specified tolerance (0.001–0.01), the data were not used. This approach ensures numerical stability and improved accuracy (Fig. 2b *vs.* S5†).

3.1.2 Mass balance closure. Instead of deducing the TOFs of N$_2$ and H$_2$ from stoichiometry, TOFs of all three species were fitted independently, without enforcing stoichiometry. While the mean absolute error for each TOF remained the same, the ratio of TOFs of NH$_3$ to H$_2$ or N$_2$ deviated from stoichiometry (Fig. S4a and b†). This
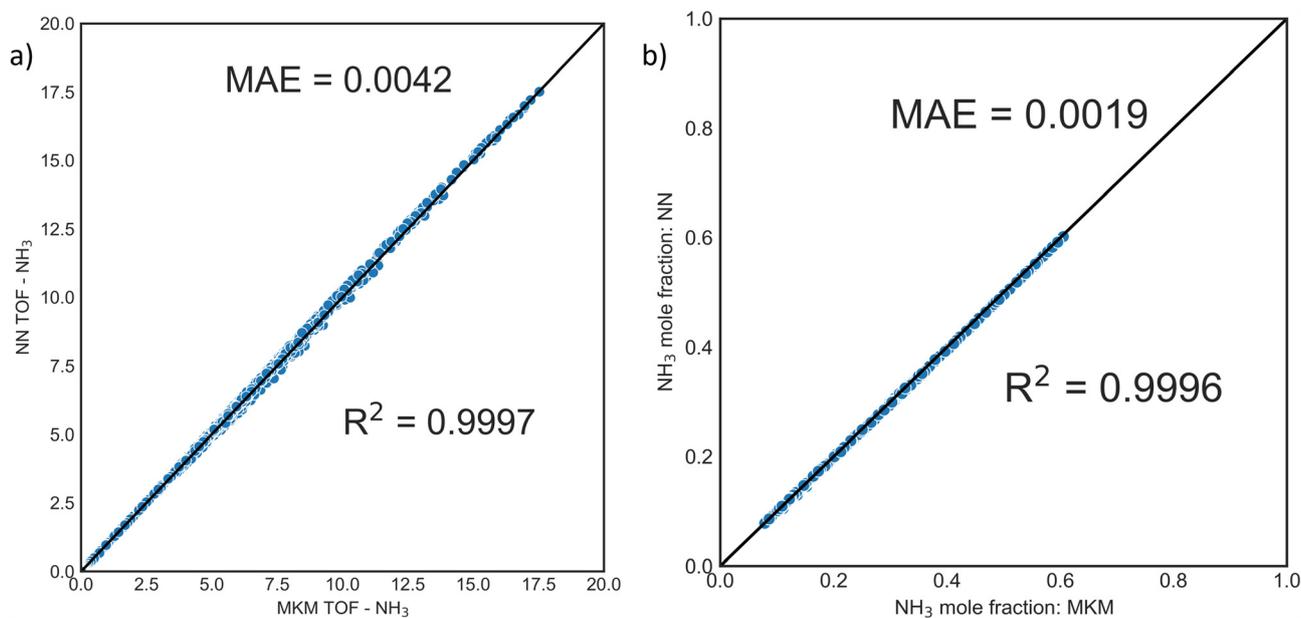

Fig. 2 Parity plots for DNN surrogate model for ammonia decomposition. a) Predicted turnover frequency (TOF) of NH$_3$ *vs.* the exact MKM. b) Exit mole fractions for NH$_3$ from 1200 PFR reactor simulations using the DNN-surrogate Python ODE solver model and the MKM (*x*-axis).

This journal is © The Royal Society of Chemistry 2024

React. Chem. Eng., 2024, **9**, 119–131 | **123**

mostly occurs at conditions close to equilibrium; see Fig. S6c and d.† Implementing a PFR-surrogate model with this DNN still resulted in accurate outcomes, as shown in Fig. S7.† Yet, we recommend not to sample too close to equilibrium.

3.1.3 Apparent activation energy. The apparent activation energy was determined using an Arrhenius plot, where log-normalized TOFs of NH_3 were plotted on the y-axis against $1000/T$ (with T in Kelvin) on the x-axis. This was done for the first CSTR reactor (PFR represented as a series of CSTRs) in both the full-order MKM and the DNN-surrogate-based model, as illustrated in Fig. S8.† The DNN model effectively captures the temperature-dependent reaction trends, revealing an apparent activation energy of 168.95 kJ mol^{-1} *vs.* 163.76 kJ mol^{-1} for the full-order MKM.

3.1.4 Sampling. In the previous example, 1200 PFR reactor simulations with 100 datapoints for each resulted in 120 000 individual samples. Smaller datasets generated using LHS and full factorial (FF) design for 100 and 400 conditions were tested. The trained DNN then predicted 400 new PFR conditions at completely random P, T, and flowrates. Parity plots of exit mole fraction using DNNs trained from samples generated by FF design and LHS are shown in Fig. 3. For a fixed number of samples, the LHS-based dataset is superior to the FF design, even with as few as 100 PFR samples (10 000 individual points).

3.2 CH$_4$ coupling chemistry

The operating window is given in the Methods section. This MKM contains 500+ species and 9300+ elementary reactions.
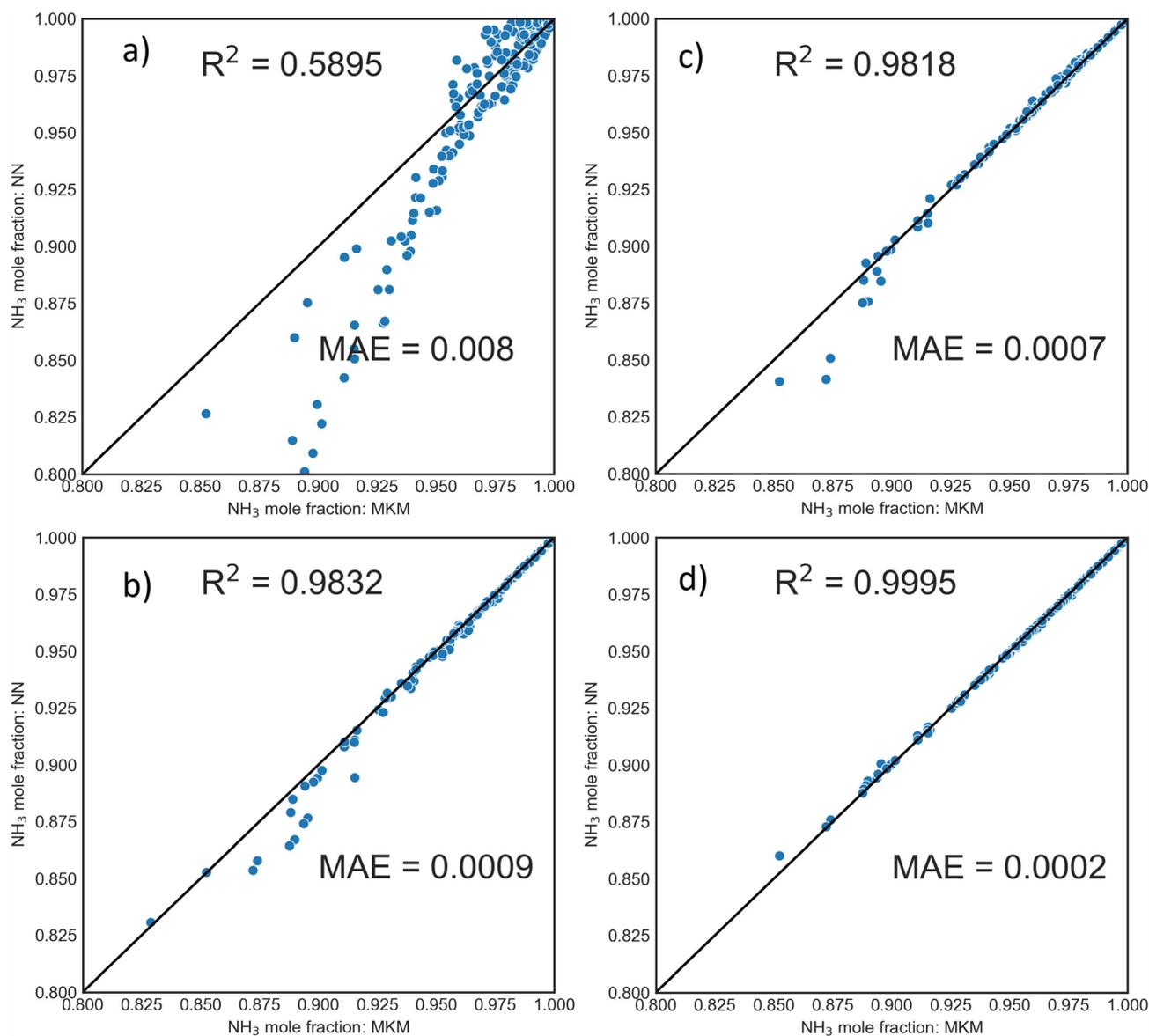

Fig. 3 Parity plots for PFR exit mole fraction for unseen, randomly chosen operating conditions within the training phase-space using DNNs trained with FF design for a) 100 and c) 400 PFR simulations or LHS sampling for b) 100 and d) 400 PFR simulations.

124 | *React. Chem. Eng.*, 2024, **9**, 119–131

This journal is © The Royal Society of Chemistry 2024

Table 1 Set of overall reactions that connect key species for non-oxidative methane coupling

No.	Reaction set A	Mathematically convenient set B
1	$2CH_4 \rightleftharpoons C_2H_4 + 2H_2$	$2CH_4 \rightleftharpoons C_2H_4 + 2H_2$
2	$3C_2H_4 \rightleftharpoons C_2H_2 + H_2$	$2CH_4 \rightleftharpoons C_2H_2 + 3H_2$
3	$2C_2H_4 + H_2 \rightleftharpoons C_3H_6 + CH_4$	$3CH_4 \rightleftharpoons C_3H_6 + 3H_2$
4	$6CH_4 \rightleftharpoons C_6H_6 + 9H_2$	$6CH_4 \rightleftharpoons C_6H_6 + 9H_2$
5	$C_3H_4 + H_2 \rightleftharpoons C_2H_2 + CH_4$	$3CH_4 \rightleftharpoons C_3H_4 + 4H_2$
6	$C_7H_8 + H_2 \rightleftharpoons C_6H_6 + CH_4$	$7CH_4 \rightleftharpoons C_7H_8 + 10H_2$
	Balance trace reactions:	Balance trace reactions:
7	$xCH_4 \rightleftharpoons C_xH_y(g) + (4x - 1.0y)H(g)$	$xCH_4 \rightleftharpoons C_xH_y(g) + (4x - 1.0y)H(g)$
8	$(4x - 1y)H(g) \rightleftharpoons (2x - 0.5y)H_2(g)$	$(4x - 1y)H(g) \rightleftharpoons (2x - 0.5y)H_2(g)$

It is impractical to fit these many TOFs. RPA (Fig. S9†) cannot even help in visualizing the network. Therefore, stable species with the largest mole fraction contribution to a cumulative ~99.5% were selected. In Fig. S10,† the cumulative histogram depicts the number of species comprising 99.5% of the PFR exit mole fraction for 200 PFR simulations, *i.e.*, at the PFR exit, 3 species make up the 99.5% cutoff for ~75 simulations, 5 species appear in ~110, and so on and so forth, up to a total of 9 unique species cumulatively for the entire dataset. Table S1† depicts the percentage of these occurrences for each key species at the PFR exit. C_2H_4 contributes to the 99.5% exit mole fraction cutoff at 60% of the training dataset (*i.e.*, 120 out of 200 PFR runs). Ultimately, the DNN surrogate model only considers 9 key species, as shown in Table S1.† The mass/mole fraction cutoff could be adjusted for every system to incorporate species of interest, including trace products or impurities.

In MKMs based on elementary reactions, short-lived species of low concentrations (for example a CH_3 radical) can play a crucial role in dictating rate-limiting steps, major flux pathways, and surface coverages. In the reduced DNN-based PFR model, we only track long-lived gas species connected by "non-elementary" overall reaction steps, such as ($2CH_4 \rightarrow C_2H_4 + 2H_2$), which do not contain these intermediates. The overall reactions encompass the information of elementary steps and intermediate species implicitly in the DNN.

3.2.1 Overall reactions. While a MKM contains all elementary reaction rates and species rates from the stoichiometric relations, it is impractical to construct overall reactions from the 9300+ elementary reactions. Instead, we propose to compute the major species rates from those of the elementary reactions and the stoichiometric relations. This approach parallels experimental efforts where species are identified, and their rates are estimated from their concentrations and basic material balances. We then introduce user-defined overall reactions that connect the major species. Determining overall reaction rates from species rates is typically an ill-posed inverse problem (solving for the rhs of eqn (3)), and the set of overall reactions is often not unique (for recent developments see ref. 68).

Two reaction sets, shown in Table 1, were chosen for this case. Set A was designed such that the reaction rates can be obtained from the respective product species, such as C_2H_4 or C_6H_6, using the stoichiometric matrix inversion. Set B was constructed using stoichiometry by which the rate of a reaction is equal to the rate of the hydrocarbon product (species rate). The last two overall reactions track the rates of CH_4 and H_2 to trace products (mole fraction <0.05) for the C and H balance. The rate of methane is easy to compute from the rates of reactions and the stoichiometric coefficients. Note that these overall reactions simply obey stoichiometry rather than physical pathways. They allow an easy estimation of rates needed in the material balances.

3.2.2 Calculating rates for overall reaction set A. For a simple system with two overall reactions connecting CH_4, C_2H_4, C_2H_2, and H_2, Fig. S11† depicts the linear set of ODEs connecting the species production rates and the overall reaction rates *via* the stoichiometric matrix. For set A of Table 1, the species and overall reaction rates are defined in Fig. 4. From MKM simulations, we can obtain the overall species production rates. Estimating the rates of overall

S - Matrix

$$
\begin{bmatrix}
\frac{drate_{H_2}}{dt} \\
\frac{drate_{C_2H_4}}{dt} \\
\frac{drate_{C_2H_2}}{dt} \\
\frac{drate_{CH_4}}{dt} \\
\frac{drate_{C_3H_6}}{dt} \\
\frac{drate_{C_6H_6}}{dt} \\
\frac{drate_{C_3H_4}}{dt} \\
\frac{drate_{C_7H_8}}{dt} \\
\frac{drate_{C-bal}}{dt} \\
\frac{drate_{H-bal}}{dt}
\end{bmatrix}_{10 \times 1}
=
\begin{bmatrix}
2 & 1 & -1 & 9 & -1 & -1 & 0 & 1 \\
1 & -1 & -2 & 0 & 0 & 0 & 0 & 0 \\
0 & 1 & 0 & 0 & 1 & 0 & 0 & 0 \\
-2 & 0 & 1 & -6 & 1 & 1 & -1 & 0 \\
0 & 0 & 1 & 0 & 0 & 0 & 0 & 0 \\
0 & 0 & 0 & 1 & 0 & 1 & 0 & 0 \\
0 & 0 & 0 & 0 & -1 & 0 & 0 & 0 \\
0 & 0 & 0 & 0 & 0 & -1 & 0 & 0 \\
0 & 0 & 0 & 0 & 0 & 0 & 1 & 0 \\
0 & 0 & 0 & 0 & 0 & 0 & 0 & -1
\end{bmatrix}_{10 \times 8}
\times
\begin{bmatrix}
rxnrate_1 \\
rxnrate_2 \\
rxnrate_3 \\
rxnrate_4 \\
rxnrate_5 \\
rxnrate_6 \\
rxnrate_7 \\
rxnrate_8
\end{bmatrix}_{8 \times 1}
$$

species_rate   **reaction_rate**

Fig. 4 Schematic of species production rates and overall reaction rates *via* the stoichiometric matrix for the reaction set A in Table 1.

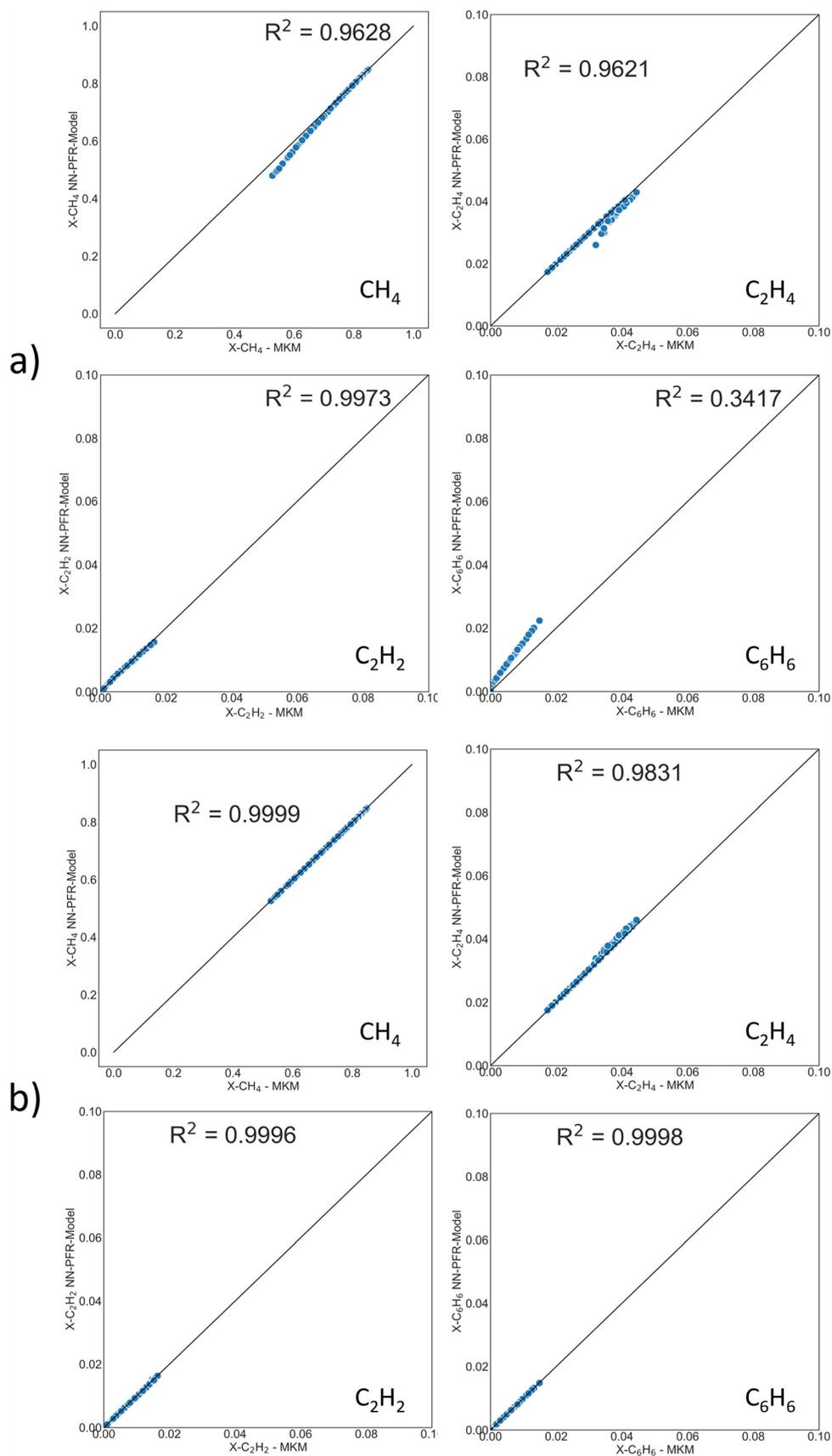This journal is © The Royal Society of Chemistry 2024

React. Chem. Eng., 2024, **9**, 119–131 | 125

Fig. 5 Parity plots of PFR exit mole fraction of CH_4, C_2H_4, C_2H_2, C_6H_6 from DNN-based surrogate model (*y*-axis) and MKM (*x*-axis) for a) reaction set A and b) reaction set B. Trace reactions are considered for both reaction sets.

126 | *React. Chem. Eng.*, 2024, **9**, 119–131

This journal is © The Royal Society of Chemistry 2024

reactions requires matrix inversion. However, the inversion problem does not always have a full rank, and techniques such as Moore–Penrose pseudo-inverse[69,70] must be used. The errors of the overall reaction rates using inversion were insignificant for reactions with high rates but can be large for those with low rate.

3.2.3 Calculating rates of overall reaction set B. Set B is mathematically convenient because the rate of each overall reaction is equal to the product species rate explicitly available from the MKM simulation; for instance, the rate of reaction 1 equals the rate of production of C_2H_4 and so forth.

3.2.4 DNN training and predictions. Fig. S12a and b† compares the overall reaction rates from MKM simulations and DNN for sets A (estimates using the inverse stoichiometric matrix) and B (exact overall rates), respectively. While the parity for both sets is fine, the results for set A are not as accurate, as shown in Fig. 5. Reducing the number of overall reactions helped minimize this error, and therefore we repeated the procedure for set A but excluded the carbon and hydrogen balance trace reactions 7 and 8. This resulted in a much more accurate surrogate model, as shown in Fig. S13,† comparable to set B. The R^2 values for the PFR exit predictions are upwards of ~0.97 and ~0.98 for all major product species for set A (without trace reactions) and set B (with trace reactions), respectively.

3.2.5 UQ in training and reactor calculations. The NN training involves randomness, and therefore NNs trained on identical data have different hyper-parameters and predictions. This uncertainty was captured by training 100 independent NNs, with identical network architecture, but initialized with randomized weights and biases, on the

previously used training dataset for the methane MKM. The overall reaction turnovers were accessed. Fig. S14† and 6 depict the uncertainty histogram with standard deviation (dotted lines) between the overall reaction TOF predictions from MKM and DNNs for 2 million data points (20 000 points per network times 100 networks) for reaction sets A (no trace reactions) and B, respectively. The mean, minimum, and the maximum for each overall reaction rate, the mean average error, and the standard deviation for the global dataset (2 million data points) are tabulated in Tables S2 (reaction set A) and S3† (reaction set B). From the UQ distribution and the tabulated statistics, the uncertainty of the NN for 100 networks is equivalent to the UQ from a single network.

Further, the propagation error and uncertainty during numerical integration of the surrogate NN models were also explored, by simulating 200 conditions with each of the independently trained NNs, for a total aggregate of 20 000 surrogate-DNN PFR simulations. Fig. S15† and 7 depict the UQ for reaction sets A and B, respectively. While the UQ histograms for H_2 and C_2H_4 are not perfectly Gaussian, the standard deviations are incredibly low, highlighting the efficacy and accuracy of this method.

3.2.6 Spatial concentration profiles for the PFR reactor. Along the length of the PFR, the spatial profiles of species mole fractions (major and minor products) predicted by the reduced model agree well with the full-order model, as shown in Fig. S16 and S17.† For primary products that convert to secondary products (*e.g.*, C_2H_4), the dynamics is also captured well. Two separate cases representing high and low conversion of CH_4 (T = 1290 K and Q = 0.026 cm^3 s^{-1} and T = 1259 K and Q = 0.098 cm^3 s^{-1}) are shown in Fig. S16 and S17.†
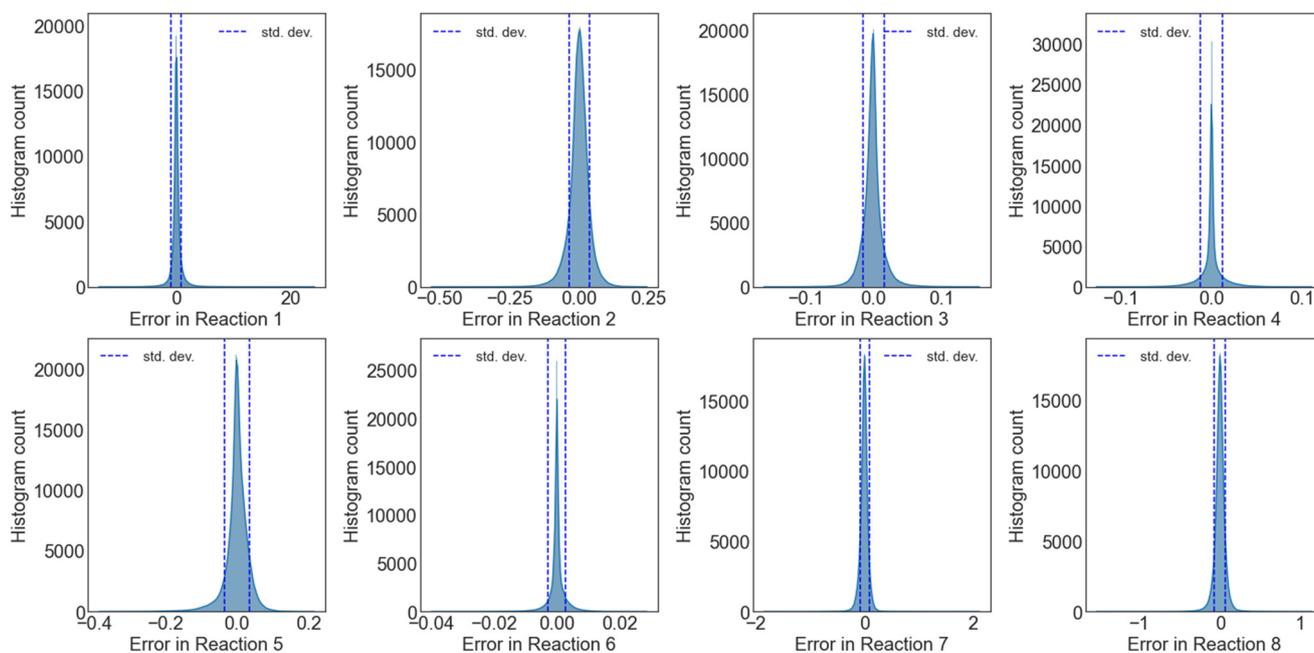

Fig. 6 Uncertainty quantification of the NN training error for a cumulative 100 independent NNs trained on reaction set B. Errors are deviations of overall rates between NN predictions and MKM calculations. Errors in rates are in 1 s^{-1}.
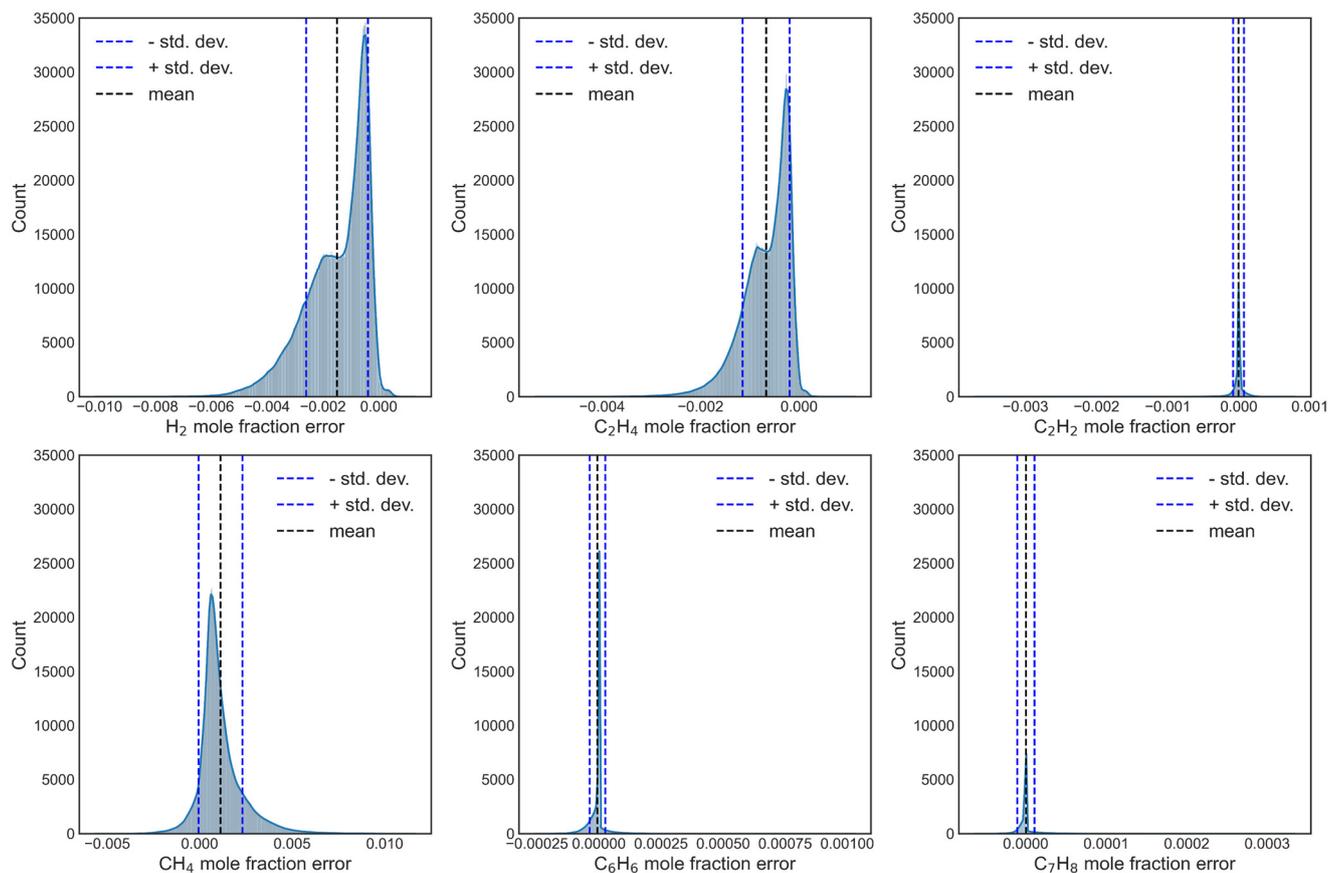
Fig. 7 DNN-based propagation error for exit mole fractions of key species for reaction set B. Each *x*-axis represents mole fraction.

3.2.7 Computational speedup and tradeoffs. The NN-based model of ammonia chemistry was reduced from 3 s in OpenMKM to 0.15 s using the Python-TensorFlow ($\sim$20 times). For CH_4 coupling, the values were 5500 s on CHEMKIN (MKM) *vs.* 3.3 s on TensorFlow-OpenMKM, a 1300-fold speedup without loss in accuracy. While the reduced model is significantly faster than the full model, the time taken for the generation of the training dataset and the training of the NNs should also be considered. Depending on the operating conditions and complexity of the model, a small number of initial full model simulations might be sufficient. In situations where the reduced NN model must be computed several times (*e.g.*, CFD), the computational benefits far outweigh the cost of training the DNN, especially for complex systems, such as methane coupling with greater than 1000-fold speedup. One other consideration is that the reduced models designed here only track long-lived gas species. If one is interested in surface coverages, the workflow has to be redefined.

4. Conclusions

We have developed a procedure to systematically reduce complex, stiff, high-dimensional chemical reaction networks using DNN models. These surrogate models approximate the rates of reactants and products only as a function of local reactor conditions and deduce rates of overall reactions connecting these species. By discarding unnecessary species (reaction intermediates and products of low fraction), the DNN-surrogate models are very small and computationally efficient with minimal (if any) stiffness. The approach was tested on a simple 14-elementary-reaction MKM for ammonia decomposition on Ru and highly complex 9300+ elementary reactions for non-oxidative methane coupling. The results demonstrate exceptional computational speed-up and accuracy. Care should be taken to use the DNN surrogate within the range of training operating conditions, and consider mass conservation, distance from chemical equilibrium, and appropriate overall reactions, as discussed herein.

Author contributions

Sashank Kasiraju developed the algorithm, performed the simulations, and wrote the manuscript. Dionisios G. Vlachos proposed the algorithm, supervised the project, wrote the manuscript, and acquired funding for this project.

Conflicts of interest

There are no conflicts to declare.

Acknowledgements

References

1 G. R. Wittreich, K. Alexopoulos and D. G. Vlachos, *Microkinetic Modeling of Surface Catalysis*, 2020, pp. 1377–1404.

2 V. Prasad, A. M. Karim, A. Arya and D. G. Vlachos, Assessment of Overall Rate Expressions and Multiscale, Microkinetic Model Uniqueness via Experimental Data Injection: Ammonia Decomposition on Ru/γ-Al2O3 for Hydrogen Production, *Ind. Eng. Chem. Res.*, 2009, **48**(11), 5255–5265.

3 J. E. Sutton and D. G. Vlachos, Building large microkinetic models with first-principles' accuracy at reduced computational cost, *Chem. Eng. Sci.*, 2015, **121**, 190–199.

4 M. Maestri, D. G. Vlachos, A. Beretta, G. Groppi and E. Tronconi, A C1microkinetic model for methane conversion to syngas on Rh/Al2O3, *AIChE J.*, 2009, **55**(4), 993–1008.

5 M. Salciccioli, M. Stamatakis, S. Caratzoulas and D. G. Vlachos, A review of multiscale modeling of metal-catalyzed reactions: Mechanism development for complexity and emergent behavior, *Chem. Eng. Sci.*, 2011, **66**(19), 4319–4355.

6 G. R. Wittreich, G. H. Gu, D. J. Robinson, M. A. Katsoulakis and D. G. Vlachos, Uncertainty Quantification and Error Propagation in the Enthalpy and Entropy of Surface Reactions Arising from a Single DFT Functional, *J. Phys. Chem. C*, 2021, **125**(33), 18187–18196.

7 V. Prasad and D. G. Vlachos, Multiscale Model and Informatics-Based Optimal Design of Experiments: Application to the Catalytic Decomposition of Ammonia on Ruthenium, *Ind. Eng. Chem. Res.*, 2008, **47**(17), 6555–6567.

8 V. Prasad, A. M. Karim, Z. Ulissi, M. Zagrobelny and D. G. Vlachos, High throughput multiscale modeling for design of experiments, catalysts, and reactors: Application to hydrogen production from ammonia, *Chem. Eng. Sci.*, 2010, **65**(1), 240–246.

9 M. Maestri and A. Cuoci, Coupling CFD with detailed microkinetic modeling in heterogeneous catalysis, *Chem. Eng. Sci.*, 2013, **96**, 106–117.

10 T. Maffei, G. Gentile, S. Rebughini, M. Bracconi, F. Manelli, S. Lipp, A. Cuoci and M. Maestri, A multiregion operator-splitting CFD approach for coupling microkinetic modeling with internal porous transport in heterogeneous catalytic reactors, *Chem. Eng. J.*, 2016, **283**, 1392–1404.

11 R. Uglietti, M. Bracconi and M. Maestri, Coupling CFD-DEM and microkinetic modeling of surface chemistry for the simulation of catalytic fluidized systems, *React. Chem. Eng.*, 2018, **3**(4), 527–539.

12 L. A. Vandewalle, G. B. Marin and K. M. Van Geem, catchyFOAM: Euler–Euler CFD Simulations of Fluidized Bed Reactors with Microkinetic Modeling of Gas-Phase and Catalytic Surface Chemistry, *Energy Fuels*, 2021, **35**(3), 2545–2561.

13 B. Partopour and A. G. Dixon, Reduced Microkinetics Model for Computational Fluid Dynamics (CFD) Simulation of the Fixed-Bed Partial Oxidation of Ethylene, *Ind. Eng. Chem. Res.*, 2016, **55**(27), 7296–7306.

14 G. D. Wehinger, M. Ambrosetti, R. Cheula, Z.-B. Ding, M. Isoz, B. Kreitz, K. Kuhlmann, M. Kutscherauer, K. Niyogi, J. Poissonnier, R. Réocreux, D. Rudolf, J. Wagner, R. Zimmermann, M. Bracconi, H. Freund, U. Krewer and M. Maestri, Quo vadis multiscale modeling in reaction engineering? – A perspective, *Chem. Eng. Res. Des.*, 2022, **184**, 39–58.

15 D. Micale, C. Ferroni, R. Uglietti, M. Bracconi and M. Maestri, Computational Fluid Dynamics of Reacting Flows at Surfaces: Methodologies and Applications, *Chem. Ing. Tech.*, 2022, **94**(5), 634–651.

16 S. H. Lam and D. A. Goussis, The CSP method for simplifying kinetics, *Int. J. Chem. Kinet.*, 1994, **26**(4), 461–486.

17 I. P. Androulakis, Kinetic mechanism reduction based on an integer programming approach, *AIChE J.*, 2000, **46**(2), 361–371.

18 I. Banerjee and M. G. Ierapetritou, Development of an adaptive chemistry model considering micromixing effects, *Chem. Eng. Sci.*, 2003, **58**(20), 4537–4555.

19 B. Bhattacharjee, D. A. Schwer, P. I. Barton and W. H. Green, Optimally-reduced kinetic models: reaction elimination in large-scale kinetic mechanisms, *Combust. Flame*, 2003, **135**(3), 191–208.

20 H. Huang, M. Fairweather, A. S. Tomlin, J. F. Griffiths and R. B. Brad, A dynamic approach to the dimension reduction of chemical kinetic schemes, in *Computer Aided Chemical Engineering*, ed. L. Puigjaner and A. Espuña, Elsevier, 2005, vol. 20, pp. 229–234.

21 A. S. Tomlin, M. J. Pilling, T. Turányi, J. H. Merkin and J. Brindley, Mechanism reduction for the oscillatory oxidation of hydrogen: Sensitivity and quasi-steady-state analyses, *Combust. Flame*, 1992, **91**(2), 107–130.

22 Y. K. Park and D. G. Vlachos, Chemistry reduction and thermokinetic criteria for ignition of hydrogen–air mixtures at high pressures, *J. Chem. Soc., Faraday Trans.*, 1998, **94**(6), 735–743.

23 S. Raimondeau, M. Gummalla, Y. K. Park and D. G. Vlachos, Reaction network reduction for distributed systems by

This journal is © The Royal Society of Chemistry 2024

React. Chem. Eng., 2024, **9**, 119–131 | 129

model training in lumped reactors: Application to bifurcations in combustion, *Chaos*, 1999, **9**(1), 95–107.

24 A. B. Mhadeshwar and D. G. Vlachos, Is the water–gas shift reaction on Pt simple?, *Catal. Today*, 2005, **105**(1), 162–172.

25 S. Deshmukh and D. Vlachos, A reduced mechanism for methane and one-step rate expressions for fuel-lean catalytic combustion of small alkanes on noble metals, *Combust. Flame*, 2007, **149**(4), 366–383.

26 S. B. Pope, Computationally efficient implementation of combustion chemistry using in situ adaptive tabulation, *Combust. Theory Modell.*, 1997, **1**(1), 41–63.

27 L. Lu and S. B. Pope, An improved algorithm for in situ adaptive tabulation, *J. Comput. Phys.*, 2009, **228**(2), 361–386.

28 J. M. Blasi and R. J. Kee, In situ adaptive tabulation (ISAT) to accelerate transient computational fluid dynamics with complex heterogeneous chemical kinetics, *Comput. Chem. Eng.*, 2016, **84**, 36–42.

29 M. A. Singer, S. B. Pope and H. N. Najm, Operator-splitting with ISAT to model reacting flow with detailed chemistry, *Combust. Theory Modell.*, 2006, **10**(2), 199–217.

30 M. Bracconi, M. Maestri and A. Cuoci, In situ adaptive tabulation for the CFD simulation of heterogeneous reactors based on operator-splitting algorithm, *AIChE J.*, 2017, **63**(1), 95–104.

31 A. Varshney and A. Armaou, in *Dynamic optimization of stochastic systems using in situ adaptive tabulation*, 2006 American Control Conference, 14-16 June 2006, 2006, p. 7.

32 A. Varshney and A. Armaou, Reduced order modeling and dynamic optimization of multiscale PDE/kMC process systems, *Comput. Chem. Eng.*, 2008, **32**(9), 2136–2143.

33 J. D. Hedengren and T. F. Edgar, In Situ Adaptive Tabulation for Real-Time Control, *Ind. Eng. Chem. Res.*, 2005, **44**(8), 2716–2724.

34 K. Hornik, M. Stinchcombe and H. White, Multilayer feedforward networks are universal approximators, *Neural Netw.*, 1989, **2**(5), 359–366.

35 A. R. Barron, Universal approximation bounds for superpositions of a sigmoidal function, *IEEE Trans. Inf. Theory*, 1993, **39**(3), 930–945.

36 J. A. Blasco, N. Fueyo, C. Dopazo and J. Ballester, Modelling the Temporal Evolution of a Reduced Combustion Chemical System With an Artificial Neural Network, *Combust. Flame*, 1998, **113**(1–2), 38–52.

37 B. A. Sen and S. Menon, Turbulent premixed flame modeling using artificial neural networks based chemical kinetics, *Proc. Combust. Inst.*, 2009, **32**(1), 1605–1611.

38 B. A. Sen and S. Menon, Linear eddy mixing based tabulation and artificial neural networks for large eddy simulations of turbulent flames, *Combust. Flame*, 2010, **157**(1), 62–74.

39 B. A. Sen, E. R. Hawkes and S. Menon, Large eddy simulation of extinction and reignition with artificial neural networks based chemical kinetics, *Combust. Flame*, 2010, **157**(3), 566–578.

40 A. J. Sharma, R. F. Johnson, D. A. Kessler and A. Moses, Deep Learning for Scalable Chemical Kinetics, *AIAA scitech 2020 forum*, 2020, p. 0181.

41 C. Chi, G. Janiga and D. Thévenin, On-the-fly artificial neural network for chemical kinetics in direct numerical simulations of premixed combustion, *Combust. Flame*, 2021, **226**, 467–477.

42 G. S. Gusmão, A. P. Retnanto, S. C. da Cunha and A. J. Medford, Kinetics-informed neural networks, *Catal. Today*, 2023, **417**, 113701.

43 W. Ji and S. Deng, Autonomous Discovery of Unknown Reaction Pathways from Data by Chemical Reaction Neural Network, *J. Phys. Chem. A*, 2021, **125**(4), 1082–1092.

44 O. Owoyele and P. Pal, ChemNODE: A neural ordinary differential equations framework for efficient chemical kinetic solvers, *Energy and AI*, 2022, **7**, 100118.

45 R. T. Chen, Y. Rubanova, J. Bettencourt and D. K. Duvenaud, Neural ordinary differential equations, *Advances in neural information processing systems*, 2018, vol. 31.

46 Y. Weng and D. Zhou, Multiscale Physics-Informed Neural Networks for Stiff Chemical Kinetics, *J. Phys. Chem. A*, 2022, **126**(45), 8534–8543.

47 S. Wang, Y. Teng and P. Perdikaris, Understanding and Mitigating Gradient Flow Pathologies in Physics-Informed Neural Networks, *SIAM J. Sci. Comput.*, 2021, **43**(5), A3055–A3081.

48 W. Ji, W. Qiu, Z. Shi, S. Pan and S. Deng, Stiff-PINN: Physics-Informed Neural Network for Stiff Chemical Kinetics, *J. Phys. Chem. A*, 2021, **125**(36), 8098–8106.

49 W. Ji and S. Deng, KiNet: A deep neural network representation of chemical kinetics, *arXiv*, 2021, preprint, arXiv:2108.00455, DOI: **10.48550/arXiv.2108.00455**.

50 F. A. Döppel and M. Votsmeier, Efficient machine learning based surrogate models for surface kinetics by approximating the rates of the rate-determining steps, *Chem. Eng. Sci.*, 2022, **262**, 117964.

51 F. A. Döppel and M. Votsmeier, Efficient neural network models of chemical kinetics using a latent asinh rate transformation, *React. Chem. Eng.*, 2023, DOI: **10.1039/D3RE00212H**.

52 Y. Huang and J. H. Seinfeld, A Neural Network-Assisted Euler Integrator for Stiff Kinetics in Atmospheric Chemistry, *Environ. Sci. Technol.*, 2022, **56**(7), 4676–4685.

53 Scikit Learn, Data preprocessing and Normalization using the MinMaxScaler, **https://scikit-learn.org/stable/modules/generated/sklearn.preprocessing.MinMaxScaler.html**, (accessed March 1, 2023).

54 S. Caratzoulas and D. G. Vlachos, Converting fructose to 5-hydroxymethylfurfural: a quantum mechanics/molecular mechanics study of the mechanism and energetics, *Carbohydr. Res.*, 2011, **346**(5), 664–672.

55 M. Abadi, A. Agarwal, P. Barham, E. Brevdo, Z. Chen, C. Citro, G. S. Corrado, A. Davis, J. Dean, M. Devin, S. Ghemawat, I. Goodfellow, A. Harp, G. Irving, M. Isard, R. Jozefowicz, Y. Jia, L. Kaiser, M. Kudlur, J. Levenberg, D. Mané, M. Schuster, R. Monga, S. Moore, D. Murray, C. Olah, J. Shlens, B. Steiner, I. Sutskever, K. Talwar, P. Tucker, V. Vanhoucke, V. Vasudevan, F. Viégas, O. Vinyals, P. Warden, M. Wattenberg, M. Wicke, Y. Yu and X. Zheng, *Large-Scale*

130 | *React. Chem. Eng.*, 2024, **9**, 119–131

This journal is © The Royal Society of Chemistry 2024

Machine Learning on Heterogeneous Systems, 2015, https://www.tensorflow.org/.

56 K. Fukushima, Cognitron: A self-organizing multilayered neural network, *Biol. Cybern.*, 1975, **20**(3–4), 121–136.

57 D. Hendrycks and K. Gimpel, Gaussian error linear units (gelus), *arXiv*, 2016, preprint, arXiv:1606.08415, DOI: 10.48550/arXiv.1606.08415.

58 S. Caratzoulas and D. G. Vlachos, Molecular dynamics study of the stabilization of the silica hexamer Si6O15(6-) in aqueous and methanolic solutions, *J. Phys. Chem. B*, 2008, **112**(1), 7–10.

59 L. Petzold, Automatic selection of methods for solving stiff and nonstiff systems of ordinary differential equations, *SIAM J. Sci. Statist. Comput.*, 1983, **4**(1), 136–148.

60 A. C. Hindmarsh, *Toward a systematized collection of ODE solvers*, Lawrence Livermore National Lab., CA (USA), 1982.

61 J. Lym, G. R. Wittreich and D. G. Vlachos, A Python Multiscale Thermochemistry Toolbox (pMuTT) for thermochemical and kinetic parameter estimation, *Comput. Phys. Commun.*, 2020, **247**, 106864.

62 G. R. Wittreich, S. Liu, P. J. Dauenhauer and D. G. Vlachos, Catalytic resonance of ammonia synthesis by simulated dynamic ruthenium crystal strain, *Sci. Adv.*, 2022, **8**(4), eabl6576.

63 B. Medasani, S. Kasiraju and D. G. Vlachos, OpenMKM: An Open-Source C++ Multiscale Modeling Simulator for Homogeneous and Heterogeneous Catalytic Reactions, *J. Chem. Inf. Model.*, 2023, **63**(11), 3377–3391.

64 H. E. Toraman, K. Alexopoulos, S. C. Oh, S. Cheng, D. Liu and D. G. Vlachos, Ethylene production by direct conversion of methane over isolated single active centers, *Chem. Eng. J.*, 2021, **420**, 130493.

65 R. J. Kee, F. M. Rupley and J. A. Miller, Chemkin-II: A Fortran chemical kinetics package for the analysis of gas-phase chemical kinetics, DOI: 10.2172/5681118, Sandia National Laboratories Report, SAND89–8009, 1989.

66 M. E. Coltrin, R. J. Kee and F. M. Rupley, *Surface CHEMKIN (Version 4. 0): A Fortran package for analyzing heterogeneous chemical kinetics at a solid-surface—gas-phase interface*, DOI: 10.2172/6128661, Sandia National Laboratories Report, SAND-90-8003B, 1991.

67 M. E. Coltrin, R. J. Kee and F. M. Rupley, Surface chemkin: A general formalism and software for analyzing heterogeneous chemical kinetics at a gas-surface interface, *Int. J. Chem. Kinet.*, 1991, **23**(12), 1111–1128.

68 M. Cohen, T. Goculdas and D. G. Vlachos, Active learning of chemical reaction networks via probabilistic graphical models and Boolean reaction circuits, *React. Chem. Eng.*, 2023, **8**(4), 824–837.

69 R. Penrose, A generalized inverse for matrices, *Math. Proc. Cambridge Philos. Soc.*, 2008, **51**(3), 406–413.

70 A. Bjerhammar, Rectangular reciprocal matrices, with special reference to geodetic calculations, *Bull Geod.*, 1951, **20**(1), 188–220.

This journal is © The Royal Society of Chemistry 2024

React. Chem. Eng., 2024, **9**, 119–131 | **131**